Available online at www.sciencedirect.com
ScienceDirect
Trans. Nonferrous Met. Soc. China 35(2025) 1109−1121
Transactions of Nonferrous Metals Society of China
www.tnmsc.cn

Effect of extrusion ratio on microstructure and mechanical properties of AZ42 alloy sheet

Song-ke XIAO[1], Xiao-jie ZHOU[1], Gang ZENG[2,3], Hong-chao XIAO[2,3], Xin-kai KANG[2,3], Xian-zheng LU[1], Xiao-min CHEN[1], Jian ZHANG[1,4]

1. Hunan Provincial Key Laboratory of Intelligent Manufacturing Technology for High-performance Mechanical Equipment, Changsha University of Science and Technology, Changsha 410114, China;
2. Hunan Provincial Key Laboratory of Advanced Aerospace Materials, CASIC (Changsha) Advanced Materials Institute Co., Ltd., Changsha 410221, China;
3. Hunan Provincial Engineering Research Center of Wrought Magnesium Alloys and Surface Protection, Changsha 410221, China;
4. SJTU−Yibin Innovation Center for Advanced Materials, Yibin 644002, China

Received 29 February 2024; accepted 10 September 2024

Abstract: The microstructure and mechanical properties of Mg−4.5Al−2.5Zn−0.3Mn−0.2Ca (wt.%, designated as AZ42) alloys in extruded (at extrusion ratios of 28, 20 and 11.5) and peak-aged states were investigated, by using optical microscopy, scanning electron microscopy, energy dispersive spectrometry and electron backscatter diffraction. The results show that extrusion produces a typical basal fiber texture and streamlines of second phases. All samples exhibit the lowest Schmid factor of basal slip (SF_b) and the superior tensile yield strength (TYS) along extrusion direction (ED). The sample with extrusion ratio of 20 exhibits the largest average grain size, but the smallest SF_b which compensates for the disadvantage of grain coarsening and maintains the strength. After being peak-aged at 175 °C for 48 h, the sample with the extrusion ratio of 20 shows the optimal TYS along all the directions, compared to the other samples. This hopes to provide useful information for optimizing the deformation parameters of the AZ42 alloys.
Key words: AZ42 alloy; extrusion ratio; Schmid factor; strength; aging-hardening

1 Introduction

Mg alloy, as the lightest engineering structural metal material, has gradually been increasing its applications in electronics, transportation, aerospace, and other fields in recent years [1−4]. Among these, Mg−Al−Zn alloys have been widely used due to their low cost and good ductility [5−7]. The addition of Al elements can weaken the texture and improve the workability of Mg alloys [8]. By regulating the content of Al and Zn elements, the strength and ductility of Mg alloys can be improved simultaneously [9]. In this context, the composition of AZ42 alloy was designed to achieve a higher strength, as it was reported that increased Al and Zn atoms in AZ31 alloy induced higher solution strengthening effect [10]. However, the strength of Mg−Al−Zn alloys is still much lower than that of most Mg−RE alloys, Al alloys, and steels, posing a significant obstacle to their wider application [7,11,12].

Compared with cast Mg alloys, deformed Mg alloys exhibit higher mechanical properties and thus

Corresponding author: Xiao-jie ZHOU, Tel: +86-731-85258625, E-mail: xjzhoucsu@163.com;
Jian ZHANG, Tel: +86-731-85258630, E-mail: zj4343@163.com
DOI: https://doi.org/10.1016/S1003-6326(24)66737-3

have been developed significantly [13−16]. Through intense plastic deformation, the grain size of Mg alloys can be refined to the micron or submicron level, and the basal texture can be weakened. Therefore, their mechanical properties are improved [17−19]. Mg alloys have poor workability, while extrusion can produce a three-dimensional compressive stress state, refine the grain, and improve the workability [20]. The alloy is subjected to higher pressure during extrusion deformation, which is conducive to eliminating defects such as porosity in the ingot, thereby effectively improving the workability of the alloy [21,22]. In addition, due to the low cost of extrusion, it has become a widely used plastic deformation method [23]. Processing parameters, notably extrusion temperature and extrusion ratio, significantly impact the microstructure and mechanical properties of Mg alloys [24].

For example, when Mg−Nd−Zn−Zr alloys were hot extruded with varying extrusion ratios of 11, 25 and 44.4, it was observed that an increase in the extrusion ratio led to improved ductility and ultimate tensile strength (UTS) [25]. However, another study on Mg−Al−Zn alloys, specifically the AZ31 alloys, revealed that the UTS and tensile yield strength (TYS) increased significantly with an increase in the extrusion ratio up to 24, but further increasing the extrusion ratio beyond this point did not significantly affect the strength [26]. Although the above studies provide some experimental basis and rationale for the effect of extrusion ratio on Mg alloys, the direct study of the effect of extrusion ratio on the microstructure and mechanical properties of AZ42 alloys has less been reported.

In this work, the microstructure and mechanical properties of the AZ42 alloy at extrusion ratios of 28, 20 and 11.5 were investigated. Then, the AZ42 alloy was subjected to aging treatment to further improve the mechanical properties. By comparing the microstructure and mechanical properties of the extruded and aged AZ42 alloy, this work aims to provide useful information for optimizing the deformation parameters of the alloys and obtaining high-performance extruded products.

2 Experimental

The as-received material was an as-homogenized ingot of AZ42 alloy with actual composition of Mg−4.5Al−2.5Zn−0.3Mn−0.2Ca (wt.%). It was extruded at an extrusion temperature of 350 °C and different extrusion ratios to obtain three groups of different materials. The specific extrusion conditions are given in Table 1.

Rectangular blocks with dimensions of 10 mm × 8 mm × 6 mm were initially cut from the as-homogenized ingot, and rectangular blocks of the same dimensions were also cut from the as-extruded sheets of three different extrusion ratios. They were polished until the surfaces of the samples were smooth and free of scratches. Subsequently, the surfaces of the samples were cleaned with distilled water. Then, the samples were electrochemically polished in a mixture of 4% perchloric acid and 96% ethanol between −30 and −40 °C, with an electrolysis voltage of 15 V and electrolysis time of 60−120 s, for the electron backscattered diffraction (EBSD) test. Prior to observation under the optical microscope (OM, JX−18A) and scanning electron microscope (SEM, Phenom G2, operated at 15 kV), which was equipped with an energy dispersive spectrometer (EDS), the samples were immersed in the solution (1 mL acetic acid + 1 mL nitric acid + 1 g oxalic acid + 100 mL water) for 10 s.

Tensile samples, with a gauge length of 24 mm and a cross-sectional area of 6 mm × 3 mm, were cut from the sheets along the extrusion direction (ED), the 45° direction and the transverse direction (TD) using wire-cutting. These samples were subjected to tensile testing on a CMT−5105GL type tensile machine at a loading rate of 1 mm/min.

The aging treatment was carried out at 175 °C, followed by air cooling. Subsequently, the samples

Table 1 Detailed parameters of different AZ42 extrusion sheets

Sample No.	Extrusion ratio	Final width/mm	Final thickness/mm	Extrusion tube diameter/mm	Extrusion temperature/°C
1	28:1	70	25	250	350
2	20:1	220	11	250	350
3	11.5:1	70	25	160	350

were finely ground using metallographic sandpaper and the microhardness was measured using HVST−1000Z semi-automatic Vickers hardness tester. At each time node, seven points were tested on the ED−ND plane, and the trimmed mean was calculated to record and analyze the effect of different extrusion ratios on the age-hardening behavior of the alloy.

3 Results and discussion

3.1 Microstructure of as-homogenized and as-extruded alloys

Figure 1 shows the sampling schematic diagram, SEM image of the as-homogenized alloy, and three-dimensional OM images of the as-extruded sheets. Compared to the as-cast alloy with a similar composition [27,28], numerous second phases are dissolved in the Mg matrix, as shown in Fig. 1(b), providing favorable conditions for subsequent extrusion. The initial grains in the as-homogenized alloy (Fig. 1(b)) are much larger than those observed on all sides in Figs. 1(c, d, e), indicating that the extrusion process significantly contributes to grain refinement. According to the literature [29], the black rod and dot in the Figs. 1(c, d, e) are identified as β-$Mg_{17}Al_{12}$ phases. However, the EDS results in Fig. 1(b) show that insoluble Al−Mn phases are predominantly located within the grain interiors, whereas the second phases present at the grain boundaries are primarily $Mg_{17}Al_{12}$ and Al_2Ca. The extrusion process causes the second phases to be streamlined along the ED. The streamlines on V-faces of Figs. 1(c, d, e) can be clearly detected, whereas the U-faces exhibit fewer streamlines. Among Figs. 1(c, d, e), Fig. 1(c) possesses the highest extrusion ratio, leading to a more complete recrystallization, which in turn results in a significantly finer grain size compared to that in Figs. 1(d, e). Regarding Fig. 1(e), despite having the lowest extrusion ratio, the grain size is still finer than that in Fig. 1(d). It is known from Table 1 that the diameter of the extrusion cylinder of Sample 3 is only 160 mm. The smaller extrusion cylinder could change the deformation temperature rise and heat dissipation [30,31], which should affect the dynamic recrystallization (DRX) behavior. Finally, the apparently counterintuitive

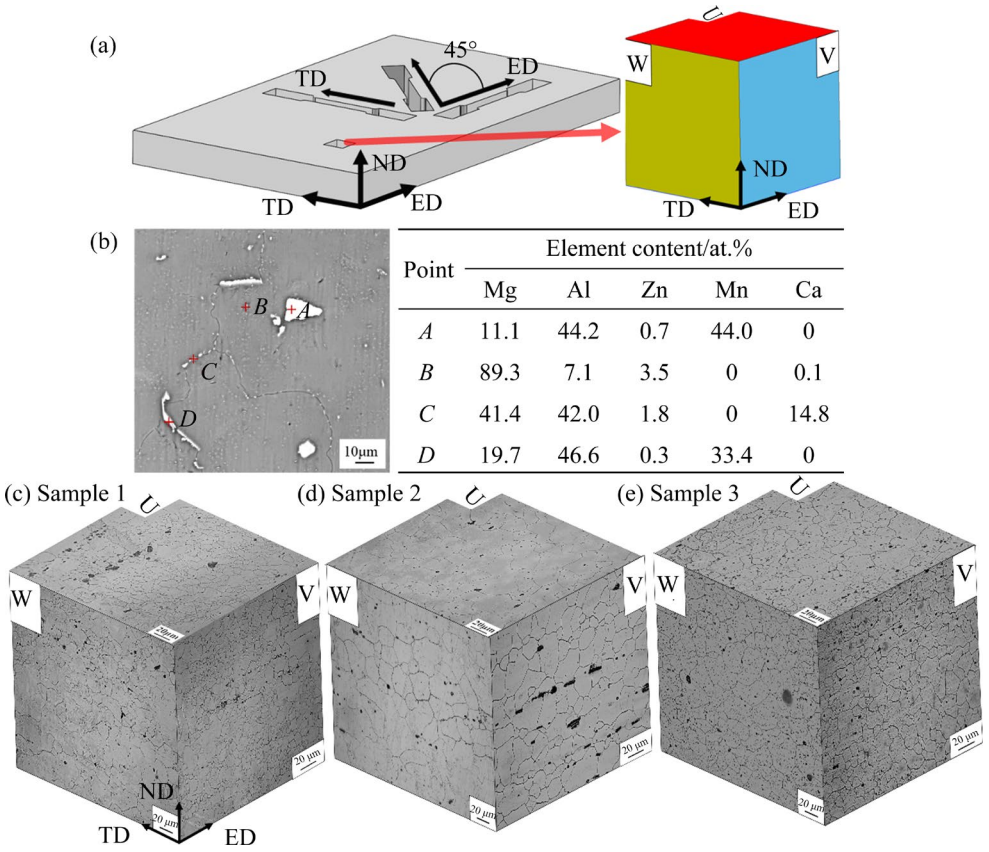

Point	Element content/at.%				
	Mg	Al	Zn	Mn	Ca
A	11.1	44.2	0.7	44.0	0
B	89.3	7.1	3.5	0	0.1
C	41.4	42.0	1.8	0	14.8
D	19.7	46.6	0.3	33.4	0

Fig. 1 Sampling schematic diagram (a), SEM image and EDS results of AZ42 as-homogenized sheet (b), and three-dimensional OM images of as-extruded sheets (c−e)

phenomenon that a smaller extrusion ratio can result in a finer average grain size can be rationalized. Furthermore, as the extrusion ratio increases, the second phases become finer and more diffusely distributed. These second phase particles, in turn, facilitate recrystallization through the particle-stimulated nucleation (PSN) mechanism. During the extrusion process, the strain accumulates near the second phase, providing a substantial driving force for the nucleation of DRXed grain and thereby activating PSN mechanism. DRXed grains preferentially nucleate around the second phase. $Mg_{17}Al_{12}$, Al−Mn and Al_2Ca phases formed by adding Al, Mn and Ca elements can promote the nucleation of DRXed grain and increase the volume fraction of fine grains. Higher extrusion ratio, therefore, provides more PSN sites, resulting in a more homogeneous microstructure [30,32].

Figure 2 shows the inverse pole figures (IPF) coloring maps of the sheets with different extrusion ratios, exhibiting average grain size of 9.6, 26.3 and 16.5 μm, respectively. The dot-like and rod-like black areas in the Fig. 2 should represent the second phases, since the EBSD software does not include information about these phases, rendering them unrecognizable and thus marked as black. Their distribution is also consistent with the OM results observed on the V-faces (see Fig. 1).

There are more red distributions in Figs. 2(a, c), indicating that the basal planes of more grains are perpendicular to the observed line of sight (i.e., TD). However, Fig. 2(b) has more green distribution, with the $\langle 11\bar{2}0\rangle$ axis parallel to the direction of view (i.e., the basal plane is parallel to the direction of view).

To further figure out the grain orientation information, the pole figures are shown in Fig. 3. The (0001) pole figures are chosen as the primary analysis object to describe the texture. It can be observed that the intensity of the pole at the center of the (0001) pole figures in Figs. 3(a, c) is higher compared to that in Fig. 3(b), indicating that the basal planes of many grains are parallel to the V-faces (see Fig. 1) of the as-extruded sheet, which corresponds to the predominance of red in Figs. 2(a, c) in the IPF map. The intensity at top and bottom ends of Fig. 3(b) is higher, indicating that the basal planes of most grains are parallel to the U-face (see Fig. 1), which corresponds to the blue-green color in Fig. 2(b) of the IPF map. Despite variations in pole distribution and intensity among the pole figure, they still represent typical characteristics of a basal fiber texture.

The recrystallization distribution maps of the sheets with different extrusion ratios are shown in Fig. 4. Red and blue represent the deformed and recrystallized grains respectively, and yellow represents the sub-grains between them. The detected DRX fractions in Figs. 4(a, b, c) are 68.3%, 63.2% and 92.5%, respectively. It has been demonstrated that DRXed grains tend to weaken, whereas deformed grains strengthen the texture [33]. In current work, the texture intensities shown in Figs. 3(a, b, c) are 8.4, 27.8 and 8.1, respectively, suggesting that the highest texture intensity of Sample 2 corresponds to its lowest DRX fraction of 63.2%, in agreement with the previously mentioned trend.

In general, the DRX fraction should increase with an increase in the extrusion ratio [33], but the value depicted in Fig. 4(a) is only 68.3%. As the extrusion ratio increases, the accumulative strain should increase. During the initial stage of metal flow in the sheet extruded at the largest extrusion ratio of 28, DRX should occur once the deformation strain reaches a critical threshold. DRXed grains should appear and occupy some regions of initial coarse grains in the as-homogenized alloy. However, at the later stage, subsequent deformation strain not only induces new DRXed grains but also introduces

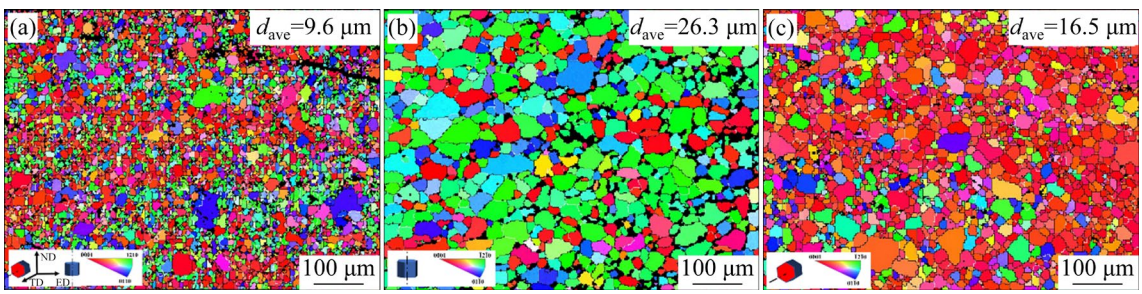

Fig. 2 Inverse pole figure (IPF) coloring maps of as-extruded sheets: (a) Sample 1; (b) Sample 2; (c) Sample 3

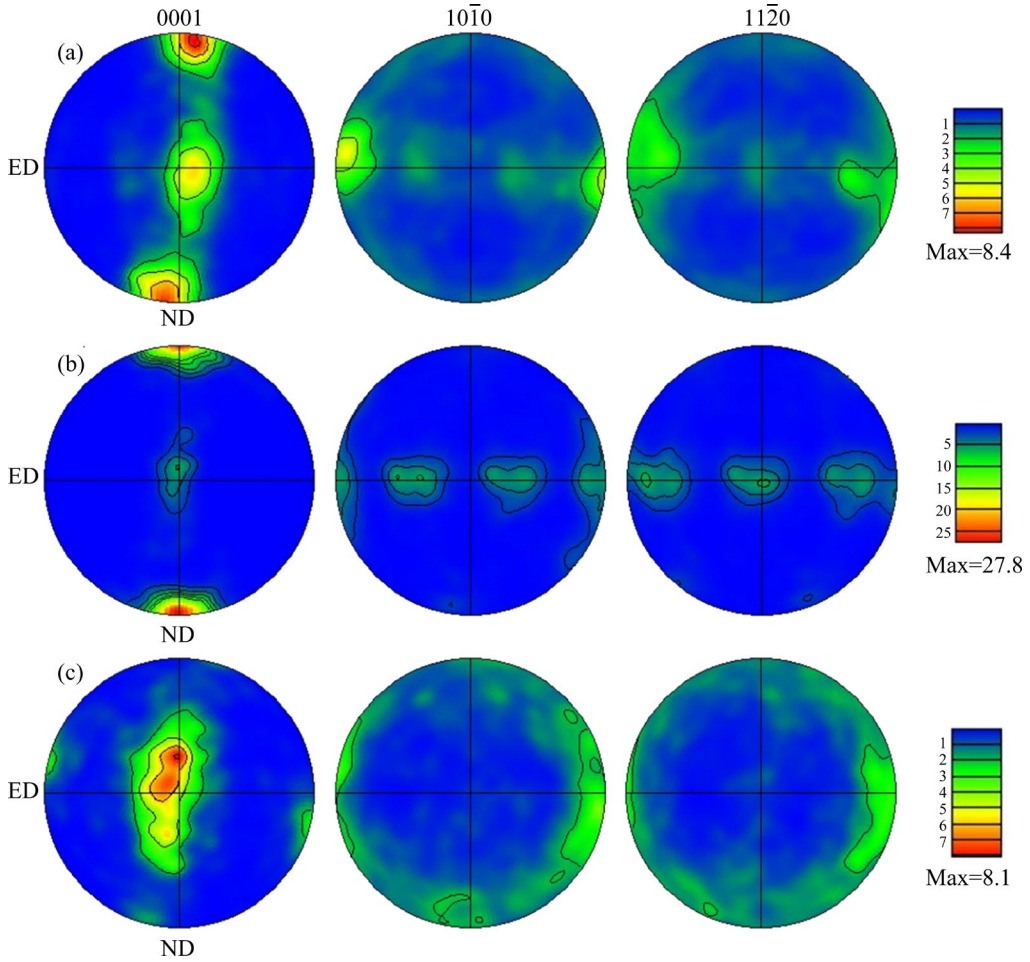

Fig. 3 Pole figures of as-extruded sheets: (a) Sample 1; (b) Sample 2; (c) Sample 3

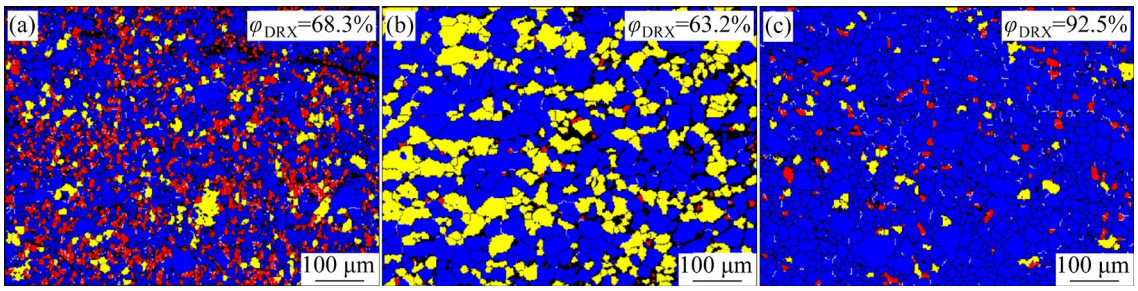

Fig. 4 Recrystallization distribution maps of as-extruded sheets: (a) Sample 1; (b) Sample 2; (c) Sample 3

more dislocations or misorientation into the initial DRXed regions (see Fig. 5), causing them to be recognized as deformed ones by the EBSD software based on the GOS (grain orientation spread) criterion [34,35]. Consequently, the actual recrystallized regions in Sample 1 may be under-estimated, which explains the weaker texture intensity observed in Fig. 3.

Sample 3 with the lowest extrusion ratio exhibits the highest DRX fraction of 92.5% and the lowest texture intensity. This should be attributed to the change of the extrusion cylinder, which could influence the deformation temperature rise or heat dissipation, and therefore promotes the DRX behavior [30,31].

The kernel average misorientation (KAM) maps are shown in Fig. 5. Indeed, Sample 1 has a larger average KAM value (i.e., higher dislocation density [36]) compared to Samples 2 and 3, suggesting that the dislocation density gradually increases with increasing extrusion ratio.

Figure 6 shows the distribution of Schmid factor of basal slip (SF_b) in different directions of as-extruded sheets. In general, the higher SF_b leads

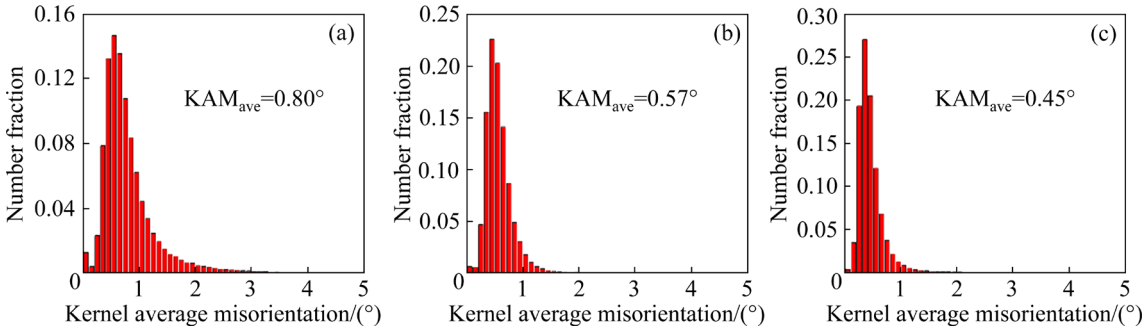

Fig. 5 KAM maps of as-extruded sheets: (a) Sample 1; (b) Sample 2; (c) Sample 3

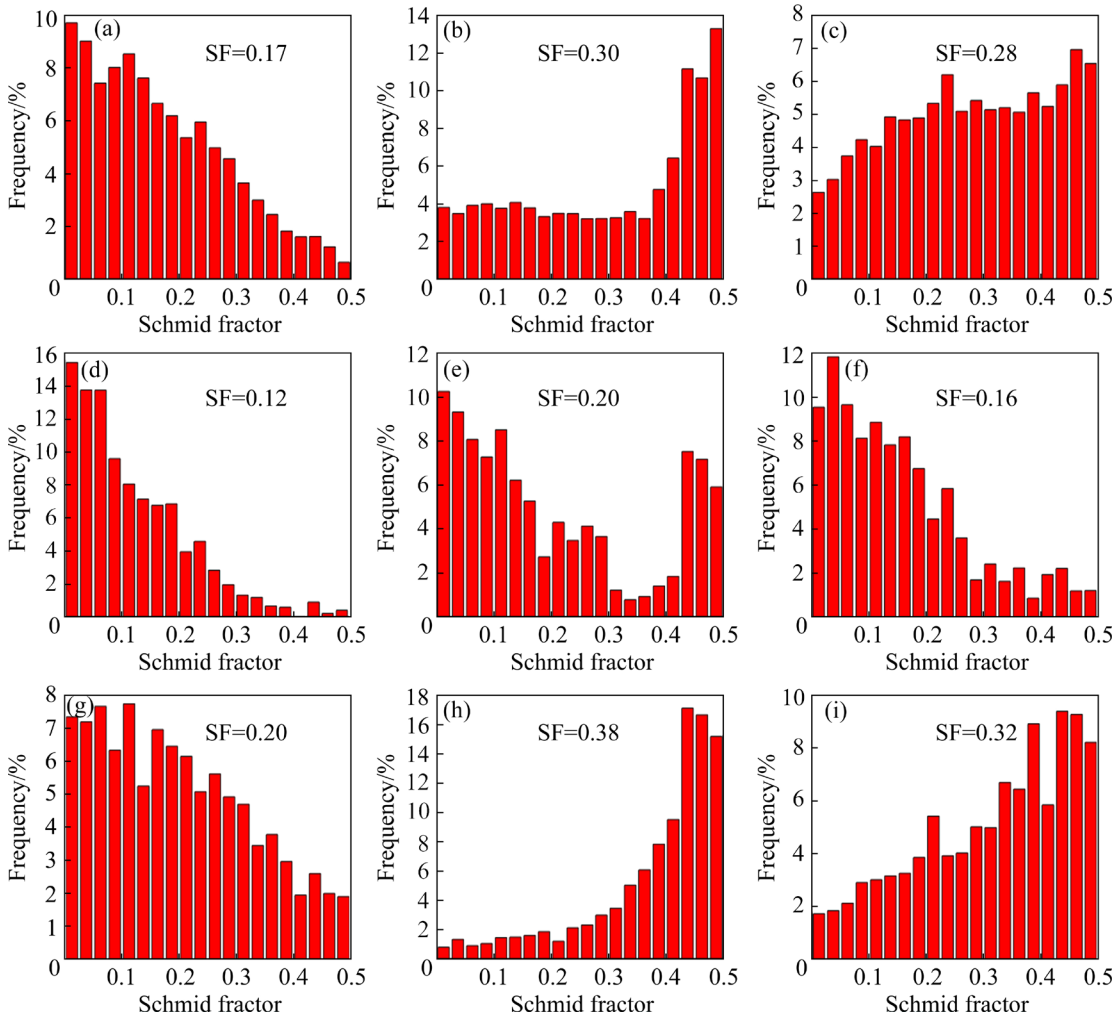

Fig. 6 Distribution of SF_b along ED (a, d, g), 45° direction (b, e, h), and TD (c, f, i) of as-extruded sheets: (a−c) Sample 1; (d−f) Sample 2; (g−i) Sample 3

to the easier basal slip with no need for a stronger loading force, i.e., lower strength. When samples in the same group are tensile tested in different directions, the SF_b is quite different. ED exhibits the lowest average SF_b (0.17, 0.12, 0.20, respectively), which is much lower than that in the 45° direction (0.30, 0.20, 0.38, respectively) and TD (0.28, 0.16, 0.32, respectively). It can be inferred that the basal slip is difficult to occur when tensile samples are tested along ED, which may lead to superior strength, followed by TD and the weakest in the 45° direction. The prediction rule is consistent with the actual measurement results (Figs. 7 and 8), indicating that the texture (or SF_b) plays a dominant role in affecting the strength of the sheets in all directions.

Interestingly, the SF_b along each direction of Sample 2 is the lowest (<0.20). According to the schematic representation of the grain orientation in the lower left corner of Fig. 2(b), the basal planes of the majority of grains are parallel to all the loading directions, which constructs the adverse condition for basal slip. Moreover, for all the as-extruded sheets, the SF_b along the 45° direction is higher than that along the other directions, since the basal planes of some grains are perpendicular to TD, as indicated by the poles at the center of the (0001) pole figures in Fig. 3. These grains own soft orientation for tensile loading along the 45° direction and contribute to enhancing the SF_b along the 45° direction.

3.2 Mechanical properties of as-extruded alloys

Figure 7 exhibits a columnar comparison of TYS, UTS and elongation (EL) of the as-extruded sheets in each tensile direction, and Fig. 8 shows the typical engineering stress−engineering strain curves. When the tensile direction is fixed, the TYS and UTS of Samples 1 and 2 are basically the same, while the EL decreases with the decrease of extrusion ratio. When the fixed sheet is tensile tested along different directions, the TYS, UTS and EL are anisotropic. The ED exhibits the highest TYS and UTS, since the lowest SF_b requires greater external loading for the operation of basal slip. The more pronounced second phase streamlines (V- and U-faces in Fig. 1) should additionally contribute to enhancing the strength [37]. The SF_b values along the 45° direction and TD for each sample are larger than those along ED (as shown in Fig. 6), which results in the lower TYS but better EL. From the comparison of Figs. 6(b, e, h) and Figs. 6(c, f, i), it can be seen that the SF_b values of TD of all the three sheets are lower than those of the 45° direction, which is consistent with the results in Fig. 7, where TYS and UTS of TD of the three sheets are higher than those along the 45° direction.

It is rationalized that the EL of Sample 2 is lower than that of the other samples in all directions due to its lower SF_b. Moreover, as shown in Fig. 1, the second phases of Sample 2 are coarser, which may promote the initiation of cracks and therefore

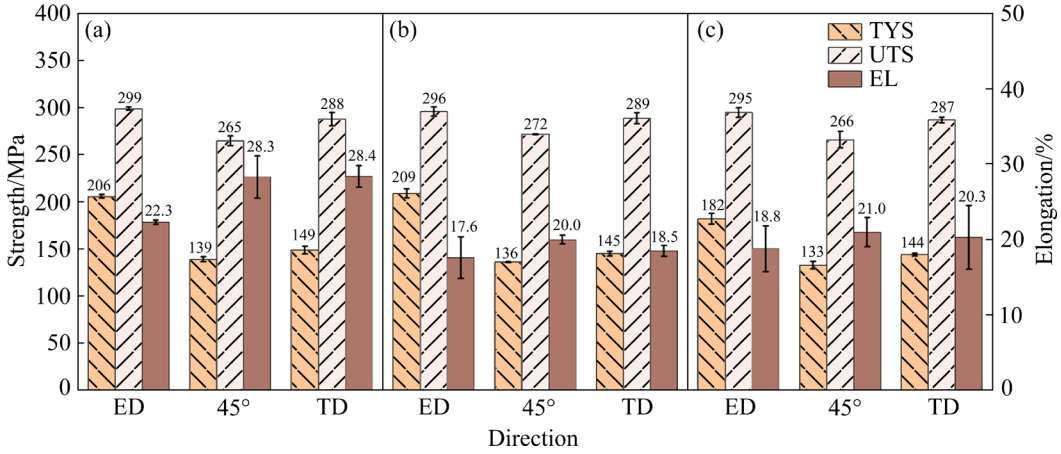

Fig. 7 Comparison of mechanical properties along different tensile directions of as-extruded sheets: (a) Sample 1; (b) Sample 2; (c) Sample 3

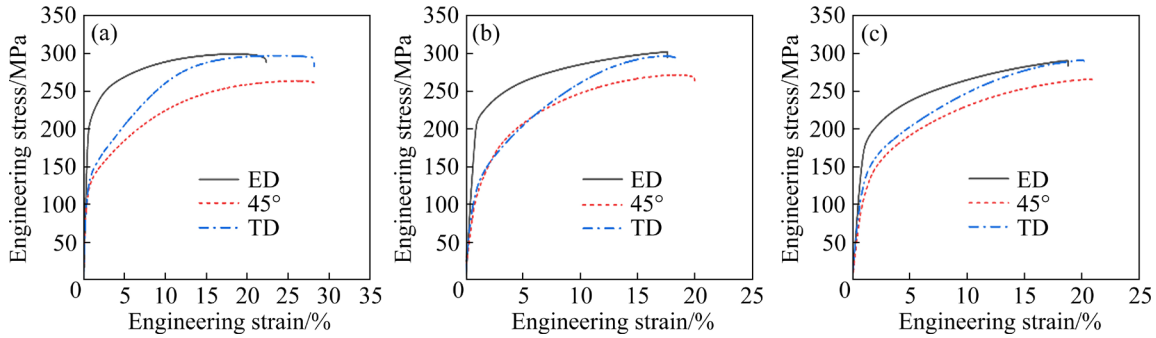

Fig. 8 Engineering stress−engineering strain curves along different tensile directions of as-extruded sheets: (a) Sample 1; (b) Sample 2; (c) Sample 3

reduce the EL [5,38]. Although Sample 2 has the largest grain size, its smaller SF_b in all directions (as shown in Fig. 6) can make up for the disadvantage of coarser grains and maintain the strength. Consequently, Sample 2 exhibits the lower ductility and higher strength.

By comparing Samples 1 and 3, the EL of Sample 3 should normally be higher than that of Sample 1, due to the weaker work-hardening effect (as can be seen in Fig. 5, Sample 1 has higher KAM value, which could reduce the EL while enhancing the strength). However, the fact is not the case. This is because Sample 1 owns the finer grain size (see Fig. 1). Then, the tensile strain could be dispersed into more grains to make the deformation more uniform, which also improves the ductility.

3.3 Aging-hardening response of as-extruded alloys

The age-hardening curves of as-extruded sheets are shown in Fig. 9. The hardness value increases slowly with the aging time at the holding temperature of 175 °C. All samples reach the peak-aged state between 40 and 50 h. As the aging time continues to extend, the hardness value rapidly decreases first and then tends to be stable.

The peak-aged hardness values of Samples 1, 2, and 3 are HV 74.2, HV 73.7, and HV 70.4, representing increases of 17.8%, 14.9%, and 15.2% compared to their initial hardness values of HV 63.0, HV 64.1, and HV 61.1, respectively. With the decrease of extrusion ratio, the peak-aged hardness value decreases. The time required for peak-aging is basically the same (46, 48, and 44 h, respectively), indicating that the extrusion ratio hardly affects the time to reach peak but has an effect on the peak-aged hardness. Moreover, it can be seen that the initial hardness of the as-extruded sheet of Sample 3 is smaller than that of Samples 1 and 2, which is consistent with the result of the TYS of each sample shown in Fig. 7.

The SEM images of AZ42 alloys with different extrusion ratios treated at 175 °C for different time of aging are shown in Fig. 10. It can be seen from Figs. 10(a−c) that compared with the as-extruded state, there are more strip and spherical second phases precipitation in the under-aged samples.

Figures 10(d−f) show the SEM images of the peak-aged samples. The $Mg_{17}Al_{12}$ phases continue to precipitate and remain mostly at the α-Mg grain boundaries, which may be beneficial to the improvement of the strength of the alloy.

Figures 10(g−i) exhibit SEM images of the over-aged (at 175 °C for 80 h) samples. Compared with the peak-aged state, the number of second phases becomes less. Some $Mg_{17}Al_{12}$ phases prefer to be discontinuously precipitated in the grain interior instead of at the grain boundaries, which not only weakens the precipitation strengthening effect, but also leads to a serious decline in the ductility of the material [39].

Figure 11 shows a columnar comparison of TYS, UTS and EL of the peak-aged AZ42 alloy sheets, and Fig. 12 shows the engineering stress−engineering strain curves of peak-aged AZ42 alloy sheets along different tensile directions.

Compared with Figs. 7 and 8, it can be seen that after peak-aging treatment, the TYS and UTS of all sheets tend to be enhanced, which is consistent with the previous conjecture that continued precipitation of the $Mg_{17}Al_{12}$ phases at grain boundaries may improve the strength. Furthermore, the TYS along the 45° direction and TD is obviously improved. It is noteworthy that the

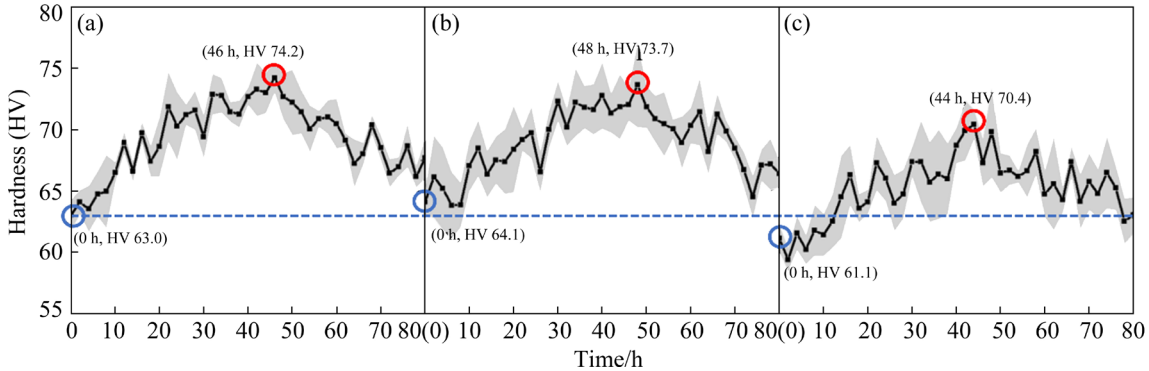

Fig. 9 Age-hardening curves of as-extruded sheets: (a) Sample 1; (b) Sample 2; (c) Sample 3

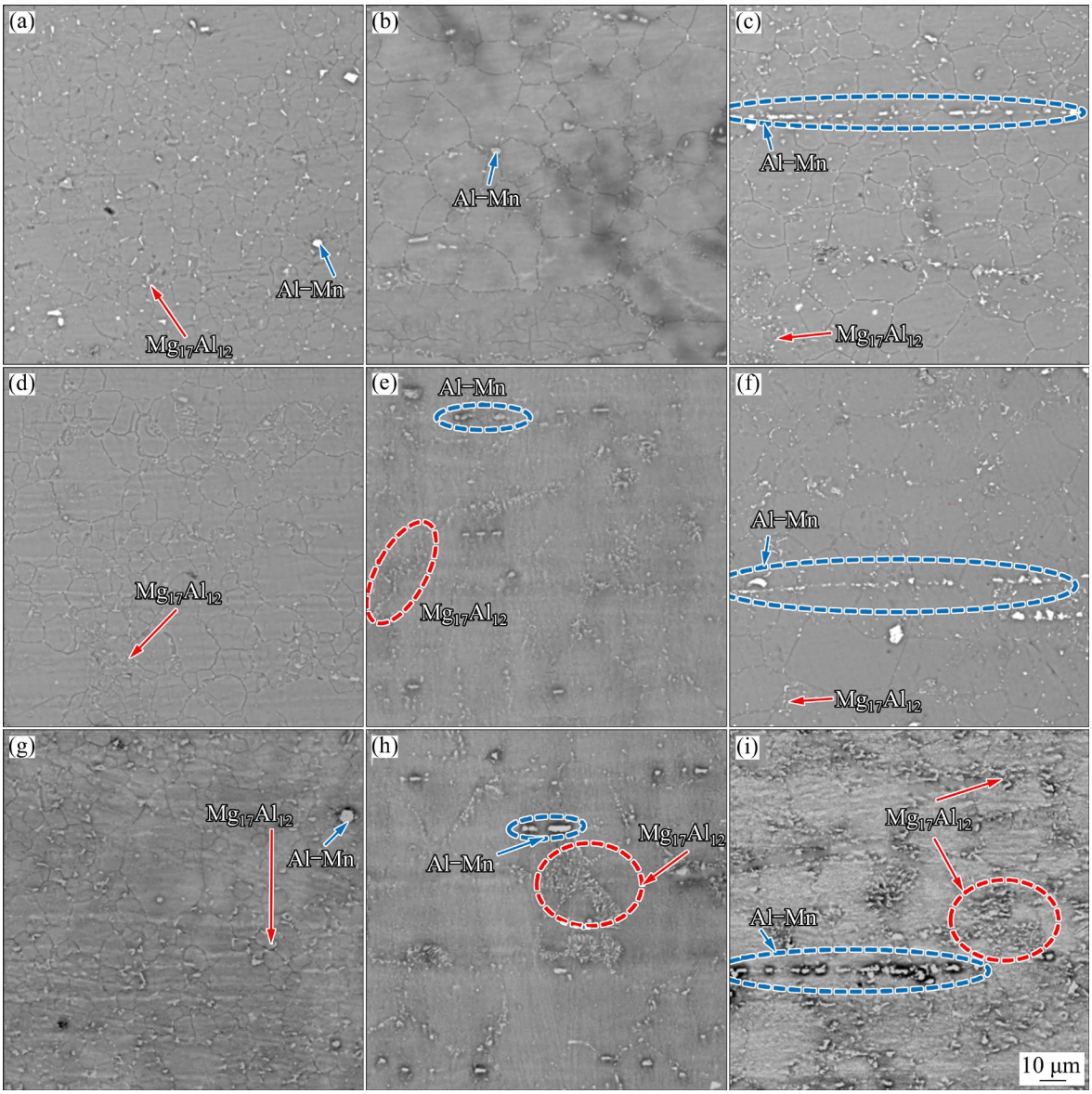

Fig. 10 SEM images of under-aged (175 °C, 20 h) (a−c), peak-aged (d−f), and over-aged (175 °C, 80 h) (g−i) AZ42 sheets: (a, d, g) Sample 1; (b, e, h) Sample 2; (c, f, i) Sample 3

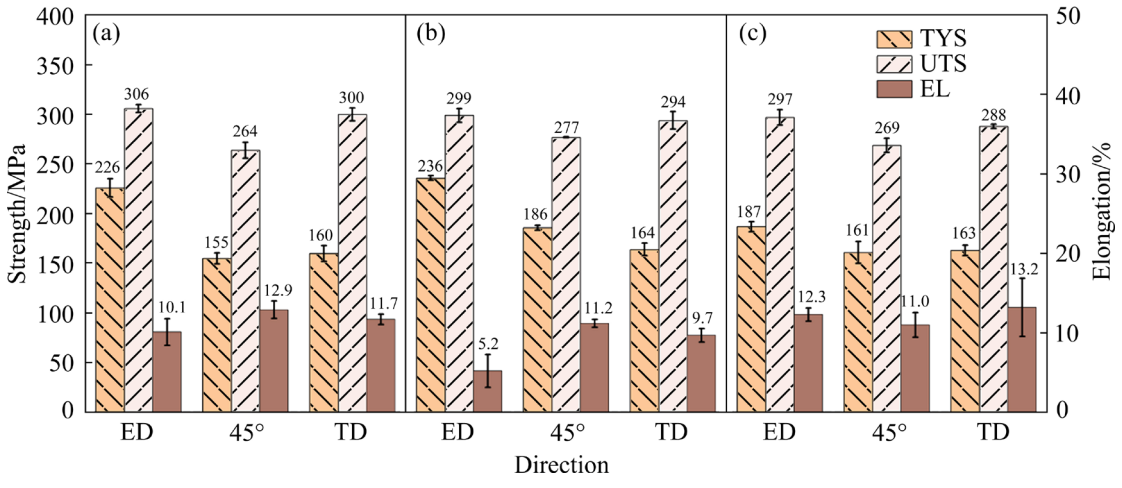

Fig. 11 Comparison of mechanical properties of peak-aged sheets: (a) Sample 1; (b) Sample 2; (c) Sample 3

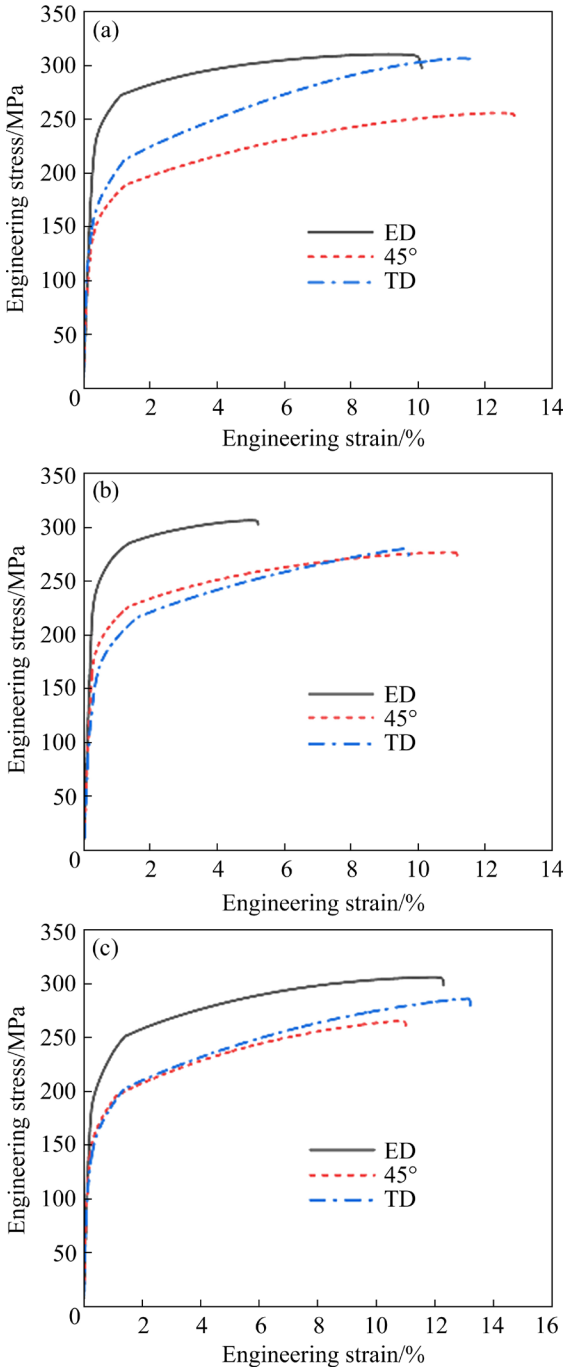

Fig. 12 Engineering stress−engineering strain curves of peak-aged sheets: (a) Sample 1; (b) Sample 2; (c) Sample 3

TYS along ED of Sample 3 (182 MPa) is slightly smaller than that of Samples 1 and 2 (206 and 209 MPa) before aging. However, after peak-aging, the TYS along ED of Sample 3 (187 MPa) increases to a much lower level than that of Samples 1 and 2 (226 and 236 MPa). This indicates that a smaller extrusion ratio is not conducive to the aging hardening of the alloy. As shown in Fig. 5, the accumulated dislocation density decreases with the reduction of deformation strain. Since dislocations can promote the diffusion and precipitation of atoms during aging [40], Sample 3 contains fewer aging precipitates and therefore exhibits lower strength compared to the other sheets. After peak-aging treatment, Sample 2 shows the optimal TYS along all the directions (236 MPa along ED, 186 MPa along 45° direction, and 164 MPa along TD).

4 Conclusions

(1) Three main second phases ($Mg_{17}Al_{12}$, Al_2Ca, and Al−Mn) are present in the as-homogenized AZ42 alloy. Extrusion at 350 °C induces the typical basal fiber texture and streamlines of second phases. Sample 1 exhibits the finest grain size of 9.6 μm.

(2) All sheets exhibit the lowest SF_b along ED, which results in the superior TYS along this direction with the assistance of second phase streamlines. Sample 2 exhibits the largest grains and the smallest SF_b. This small SF_b compensates for the disadvantage of grain coarsening and maintains the strength.

(3) As the extrusion ratio increases, the alloy shows better work-hardening effect, finer grains, and improved strength and ductility. The sheet with the extrusion ratio of 28 results in the TYS of 206 MPa and EL of 22.3% along ED, TYS of 139 MPa and EL of 28.3% along the 45° direction, and TYS of 149 MPa and EL of 28.4% along TD, respectively.

(4) The AZ42 sheets show a gradual increase in the quantity of second phases as aging treatment progresses. Additionally, at over-aging state, discontinuous precipitates tend to appear within the interior of α-Mg grains. The sheet of peak-aged (175 °C, 48 h) Sample 2 exhibits the optimal TYS along all the directions (236 MPa along ED, 186 MPa along 45° direction, and 164 MPa along TD) compared to the other sheets.

CRediT authorship contribution statement

Song-ke XIAO: Investigation, Writing − Original draft, Writing − Review & editing; **Xiao-jie ZHOU:** Investigation, Writing − Review & editing, Funding acquisition, Supervision; **Gang ZENG:** Investigation, Conceptualization, Writing − Original draft; **Hong-chao**

XIAO: Investigation, Writing − Review & editing; **Xin-kai KANG:** Investigation, Resources; **Xian-zheng LU:** Investigation, Visualization; **Xiao-min CHEN:** Investigation, Resources; **Jian ZHANG:** Investigation, Resources, Supervision.

Declaration of competing interest

The authors declare that they have no known competing financial interests or personal relationships that could have appeared to influence the work reported in this paper.

Acknowledgments

This work was supported by the National Natural Science Foundation of China (No. 51904036), the Hunan Provincial Key Research and Development Program, China (No. 2023GK2049), Changsha Municipal Natural Science Foundation, China (Nos. kq2402016, kq2402014), the Postgraduate Scientific Research Innovation Project of Hunan Province, China (No. CX20240772), and the Sichuan Science and Technology Program, China (No. 2024NSFSC0151).

References

[1] POLLOCK T M. Weight loss with magnesium alloys [J]. Science, 2010, 328: 986−987.

[2] CHENG Yuan-fen, DU Wen-bo, LIU Ke, FU Jun-jian, WANG Zhao-hui, LI Shu-bo, FU Jin-long. Mechanical properties and corrosion behaviors of Mg−4Zn−0.2Mn−0.2Ca alloy after long term in vitro degradation [J]. Transactions of Nonferrous Metals Society of China, 2020, 30: 363−372.

[3] XU Wan-qiang, BIRBILIS N, SHA Gang, WANG Yu, DANIELS J E, XIAO Yang, FERRY M. A high-specific-strength and corrosion-resistant magnesium alloy [J]. Nature Materials, 2015, 14: 1229−1235.

[4] HE J H, ZHANG J, ZHOU X J, CHEN J N, YU L P, JIANG L K, LU X Z, CHEN X M, ZHOU D W. Hydrogen storage properties of $Mg_{98.5}Gd_1Zn_{0.5}$ and $Mg_{98.5}Gd_{0.5}Y_{0.5}Zn_{0.5}$ alloys containing LPSO phases [J]. International Journal of Hydrogen Energy, 2021, 46: 32949−32961.

[5] JUNG J G, PARK S H, YU H, KIM Y M, LEE Y K, YOU B S. Improved mechanical properties of Mg−7.6Al−0.4Zn alloy through aging prior to extrusion [J]. Scripta Materialia, 2014, 93: 8−11.

[6] LIU Lin-tao, BAI Sheng-wen, JIANG Bin, HE Chao, WANG Qing-hang, YUAN Ming, HUANG Guang-sheng, ZHANG Ding-fei, PAN Fu-sheng. Improved mechanical properties of Mg−3Al−1Zn alloy sheets with TD-preferred texture prepared via turned bearing extrusion [J]. Transactions of Nonferrous Metals Society of China, 2023, 33: 2955−2969.

[7] KIM Y J, KIM S H, LEE J U, CHOI J O, KIM H S, KIM Y M, KIM Y, PARK S H. Effects of cold pre-forging on microstructure and tensile properties of extruded AZ80 alloy [J]. Materials Science and Engineering A, 2017, 708: 405−410.

[8] HUANG Xin-sheng, SUZUKI K, CHINO Y, MABUCHI M. Influence of aluminum content on the texture and sheet formability of AM series magnesium alloys [J]. Materials Science and Engineering A, 2015, 633: 144−153.

[9] GUO Fei, ZHANG Ding-fei, WU Hua-yi, JIANG Lu-yao, PAN Fu-sheng. The role of Al content on deformation behavior and related texture evolution during hot rolling of Mg−Al−Zn alloys [J]. Journal of Alloys and Compounds, 2017, 695: 396−403.

[10] MA Chen-yi, XIA Nan, WANG Cheng, LI Mei-xuan, HUA Zhen-ming, REN Ming-wen, WANG Hui-yuan. A novel Mg−5Al−2Zn−2Sn alloy with high strength-ductility synergy fabricated via simple hot rolling and annealing treatment [J]. Journal of Alloys and Compounds, 2021, 869: 159308.

[11] BAE S W, KIM S H, LEE J U, JO W K, HONG W H, KIM W, PARK S H. Improvement of mechanical properties and reduction of yield asymmetry of extruded Mg−Al−Zn alloy through Sn addition [J]. Journal of Alloys and Compounds, 2018, 766: 748−758.

[12] PARK S H, KIM S H, KIM Y M, YOU B S. Improving mechanical properties of extruded Mg−Al alloy with a bimodal grain structure through alloying addition [J]. Journal of Alloys and Compounds, 2015, 646: 932−936.

[13] KLEINER S, UGGOWITZER P J. Mechanical anisotropy of extruded Mg−6%Al−1%Zn alloy [J]. Materials Science and Engineering A, 2004, 379: 258−263.

[14] ZHANG Kun-ming, QIN Chen, SHE Jia, JING Xue-rui, PENG Peng, TANG Ai-tao, RASHAD M, PAN Fu-sheng. Simultaneous improvement in strength and ductility of extruded Mg alloy via novel closed forging extrusion [J]. Transactions of Nonferrous Metals Society of China, 2022, 32: 2866−2876.

[15] BARNETT M R, KESHAVARZ Z, BEER A G, ATWELL D. Influence of grain size on the compressive deformation of wrought Mg−3Al−1Zn [J]. Acta Materialia, 2004, 52: 5093−5103.

[16] GU Guang-lin, KE Xiang-nan, HU Fa-ping, ZHAO Shu-jie, WEI Guo-bin, YANG Yan, PENG Xiao-dong, XIE Wei-dong. Fine-grained Mg−1Mn−0.5Al−0.5Ca−0.5Zn alloy with high strength and good ductility fabricated by conventional extrusion [J]. Transactions of Nonferrous Metals Society of China, 2022, 32: 483−492.

[17] KAI M, HORITA Z, LANGDON T G. Developing grain refinement and superplasticity in a magnesium alloy processed by high-pressure torsion [J]. Materials Science and Engineering A, 2008, 488: 117−124.

[18] ZHOU Xiao-jie, XIA Hai-you, ZHANG Jian, ZENG Gang, LU Xian-zheng, CHEN Xiao-min, PANG Xiao-tong, LI Jia-hao, GUO Jing. Effect of ECAP temperature and deformation route on mechanical properties of pre-extruded Mg−5Gd−3Y−1Zn−0.5Zr alloys [J]. Journal of Materials Science & Technology, 2025, 212: 237−250.

[19] LIANG Min-jie, ZHENG Jie, LIU Huan, YAO Bao-xing. Microstructure and mechanical properties of AZ31 alloy prepared by cyclic expansion extrusion with asymmetrical extrusion cavity [J]. Transactions of Nonferrous Metals Society of China, 2022, 32: 122−133.

[20] BEAUSIR B, BISWAS S, KIM D I, TÓTH L S, SUWAS S. Analysis of microstructure and texture evolution in pure magnesium during symmetric and asymmetric rolling [J]. Acta Materialia, 2009, 57: 5061−5077.

[21] CHINO Y, SASSA K, MABUCHI M. Texture and stretch formability of Mg−1.5mass%Zn−0.2mass%Ce alloy rolled at different rolling temperatures [J]. Materials Transactions, 2008, 49: 2916−2918.

[22] WU Xiao-feng, XU Chun-xiang, ZHANG Zheng-wei, YANG Wen-fu, ZHANG Jing-shan. Microstructure evolution, strengthening mechanisms and deformation behavior of high-ductility Mg−3Zn−1Y−1Mn alloy at different extrusion temperatures [J]. Transactions of Nonferrous Metals Society of China, 2023, 33: 422−437.

[23] BAGHERPOUR E, PARDIS N, REIHANIAN M, EBRAHIMI R. An overview on severe plastic deformation: Research status, techniques classification, microstructure evolution, and applications [J]. The International Journal of Advanced Manufacturing Technology, 2019, 100: 1647−1694.

[24] ZHOU Shi-hao, WEI Fu-an, WANG Jin-hui, JIN Pei-peng. Effect of extrusion ratio on microstructure and mechanical properties of Mg−6Sn−3Al−1Zn alloy [J]. Materials Research Express, 2022, 9: 096517.

[25] WEN Li-hua, JI Ze-sheng, LI Xiao-liang. Effect of extrusion ratio on microstructure and mechanical properties of Mg−Nd−Zn−Zr alloys prepared by a solid recycling process [J]. Materials Characterization, 2008, 59: 1655−1660.

[26] CHEN Yong-jun, WANG Qu-dong, PENG Jian-guo, ZHAI Chun-quan, DING Wen-jiang. Effects of extrusion ratio on the microstructure and mechanical properties of AZ31 Mg alloy [J]. Journal of Materials Processing Technology, 2007, 182: 281−285.

[27] MELIA M A, SERRON M L, FLORIAN D C, WEILER J P, SCULLY J R, FITZGERALD J M. Excimer laser processing of cast Mg−Al−Zn (AZ91D) and Mg−Al (AM60B) alloys for improved corrosion resistance [J]. Corrosion, 2016, 72: 1580−1586.

[28] ZHANG Bao-hong, ZHANG Zhi-min. Influence of homogenizing on mechanical properties of as-cast AZ31 magnesium alloy [J]. Transactions of Nonferrous Metals Society of China, 2010, 20: s439−s443.

[29] LASER T, HARTIG C, NÜRNBERG M R, LETZIG D, BORMANN R. The influence of calcium and cerium mischmetal on the microstructural evolution of Mg−3Al−1Zn during extrusion and resulting mechanical properties [J]. Acta Materialia, 2008, 56: 2791−2798.

[30] DING Han-lin, LIU Liu-fa, KAMADO S, DING Wen-jiang, KOJIMA Y. Study of the microstructure, texture and tensile properties of as-extruded AZ91 magnesium alloy [J]. Journal of Alloys and Compounds, 2008, 456: 400−406.

[31] LI Na-li, HUANG Guang-jie, XIN Ren-long, LIU Qing. Influence of extrusion ratio on microstructure and texture developments of high-temperature extruded AZ31 Mg alloy [J]. Science China Technological Sciences, 2012, 55: 490−495.

[32] JIN Zhong-zheng, ZHA Min, WANG Si-qing, WANG Shi-chao, WANG Cheng, JIA Hai-long, WANG Hui-yuan. Alloying design and microstructural control strategies towards developing Mg alloys with enhanced ductility [J]. Journal of Magnesium and Alloys, 2022, 10: 1191−1206.

[33] ZHOU Xiao-jie, LIU Chu-ming, GAO Yong-hao, JIANG Shu-nong, LIU Wen-hui, LU Li-wei. Microstructure and mechanical properties of extruded Mg−Gd−Y−Zn−Zr alloys filled with intragranular LPSO phases [J]. Materials Characterization, 2018, 135: 76−83.

[34] YANG Xiao-dong, ZHOU Xiao-jie, YU Shi-lun, ZHANG Jian, LU Xian-zheng, CHEN Xiao-min, LU Li-wei, HUANG Wei-ying, LIU Ya-ru. Tensile behavior at various temperatures of the Mg−Gd−Y−Zn−Zr alloys with different initial morphologies of LPSO phases prior to extrusion [J]. Materials Science and Engineering A, 2022, 851: 143634.

[35] ZHOU Xiao-jie, XIONG Wen-ying, ZENG Gang, XIAO Hong-chao, ZHANG Jian, LU Xian-zheng, CHEN Xiao-min. Combined effects of LPSO orientation and α-Mg texture on tensile anisotropy of an extruded Mg−Gd−Y−Zn−Zr alloy [J]. Materials Science and Engineering A, 2021, 805: 140596.

[36] CHEN Xiao-min, LU Yu-feng, NING Meng-tao, ZHOU Xiao-jie, CHEN Jian. Tailoring microstructural evolution and fracture damage behavior of a Mg−Y−Zn alloy during hot tensile deformation [J]. Materials Science and Engineering A, 2023, 871: 144857.

[37] HAGIHARA K, KINOSHITA A, SUGINO Y, YAMASAKI M, KAWAMURA Y, YASUDA H Y, UMAKOSHI Y. Effect of long-period stacking ordered phase on mechanical properties of Mg97Zn1Y2 extruded alloy [J]. Acta Materialia, 2010, 58: 6282−6293.

[38] ZHOU Xiao-jie, ZHANG Jian, CHEN Xiao-min, ZHANG Xu, LI Meng-jia. Fabrication of high-strength AZ80 alloys via multidirectional forging in air with no need of ageing treatment [J]. Journal of Alloys and Compounds, 2019, 787: 551−559.

[39] YE Jie, LIN Xiao-ping, ZHAO Tian-bo, LIU Ning-ning, XIE Hong-bin, NIU Yi, TENG Fei. Influence of pre-strain on the aging hardening effect of the Mg−9.02Zn−1.68Y alloy [J]. Materials Science and Engineering A, 2016, 663: 49−55.

[40] ZHU S M, GIBSON M A, NIE J F, EASTON M A, ABBOTT T B. Microstructural analysis of the creep resistance of die-cast Mg−4Al−2RE alloy [J]. Scripta Materialia, 2008, 58: 477−480.

挤压比对 AZ42 合金板材显微组织和力学性能的影响

肖淞珂[1]，周小杰[1]，曾 钢[2,3]，肖宏超[2,3]，康心锴[2,3]，卢先正[1]，陈小敏[1]，张 健[1,4]

1. 长沙理工大学 机械装备高性能智能制造关键技术湖南省重点实验室，长沙 410114；
2. 航天科工(长沙)新材料研究院有限公司 航空新材料湖南省重点实验室，长沙 410114；
3. 湖南省变形镁合金材料及表面防护工程技术研究中心，长沙 410221
4. 上海交通大学−宜宾先进材料创新中心，宜宾 644002

摘 要：采用光学显微镜、扫描电镜、能量色散谱和背散射电子衍射等方法研究了 Mg−4.5Al−2.5Zn−0.3Mn−0.2Ca (质量分数，%，AZ42)合金在挤压(挤压比为 28、20 和 11.5)和峰时效状态下的显微组织和力学性能。结果表明：挤压过程产生典型的基面纤维织构和第二相组织，所有沿挤压方向(ED)的样品均表现出最低的基面滑移施密特因子(SF_b)和优异的拉伸屈服强度(TYS)。当挤压比为 20 时，试样平均晶粒尺寸最大，但 SF_b 最小，弥补了晶粒粗化的缺点并维持了强度。175 ℃峰时效 48 h 后，挤压比为 20 的试样在各方向上的 TYS 均优于其他试样。这为 AZ42 合金的变形工艺参数优化提供参考。

关键词：AZ42 合金；挤压比；施密特因子；强度；时效硬化

(Edited by Bing YANG)